



Contents lists available at ScienceDirect

Journal of the Mechanics and Physics of Solids

journal homepage: www.elsevier.com/locate/jmps

Beaded fiber composites—Stiffness and strength modeling

Israel Greenfeld*, Carol W. Rodricks, XiaoMeng Sui, H. Daniel Wagner*

Department of Materials and Interfaces, Weizmann Institute of Science, Rehovot 76100, Israel

ARTICLE INFO

Article history:

Received 3 September 2018

Revised 11 December 2018

Accepted 24 December 2018

Available online 28 December 2018

Keywords:

Composite

Fiber reinforcement

Intermittent beading

Beaded fiber

Shear lag

ABSTRACT

We present a theoretical analysis of the elastic stresses in a composite reinforced with beaded fibers by extending the classic Cox shear lag theory. The motivation for reinforcing a composite with beaded fibers is to improve both strength and toughness, two often conflicting properties. It is found that owing to their geometry beads intermittently placed on a fiber enhance fiber anchoring in the matrix, and can potentially dissipate energy by deforming the matrix during failure. The composite stiffness is shown to improve compared to a composite with beadless fibers, particularly when the beads are large and stiffer than the surrounding matrix. The stress profiles in the fiber, bead, matrix and along their respective interfaces incur periodic perturbations induced by the beads, modeled by Hill equation. For given elastic constants and bead geometry, these profiles reveal the weakest link loci in the structure, and consequently determine the composite strength and failure mode. A finite element analysis is presented that confirms our results. The bead-fiber and bead-matrix interfaces may be tuned by choice of materials and coatings to achieve desired mechanical properties.

© 2019 The Authors. Published by Elsevier Ltd.
This is an open access article under the CC BY license.
(<http://creativecommons.org/licenses/by/4.0/>)

1. Introduction

Achieving simultaneous stiffness, strength and toughness in synthetic materials at all size scales is an ongoing challenge in research and engineering, and compromises are unavoidable (Ritchie, 2011; Tsai et al., 1990; Yang et al., 2016). In biology, hierarchical composite structures such as bone and wood suggest a strategy based on a multilevel design, from nanoscale to macroscale (Barthelat et al., 2016; Greenfeld et al., 2016; Greenfeld and Wagner, 2015; Sui et al., 2016; Sui and Wagner, 2009; Wegst et al., 2015; Weiner and Wagner, 1998). Fiber reinforced composites suffer from the same dichotomy: a strong fiber-matrix interface guarantees high composite strength but low toughness, whereas a weak interface dissipates more energy during deformation and thereby benefits toughness but induces lower strength (Cottrell, 1964; Greenfeld and Wagner, 2015; Kelly, 1970). To solve this conflict, structural variations such as bone-shaped fibers and intermittent bonding have been suggested (Atkins, 1975; Bagwell and Wetherhold, 2003; Beyerlein et al., 2001; Gao et al., 2011; Jensen and McKnight, 2006; Phanthien, 1981; Wetherhold et al., 2007; Wetherhold and Lee, 2001; Zhu et al., 1998).

Recently, we introduced the concept of intermittent beading, in which the composite is reinforced by beaded fibers (Greenfeld et al., 2018) (Fig. 1). The beads serve as topological anchors of the fibers in the matrix, transmit the stress from the matrix to the fibers more efficiently, and absorb energy by deforming the matrix during failure. Thus, beaded fibers have the potential of improving both strength and toughness in a given fiber-matrix system.

* Corresponding authors.

E-mail addresses: green_is@netvision.net.il (I. Greenfeld), Daniel.Wagner@weizmann.ac.il (H.D. Wagner).

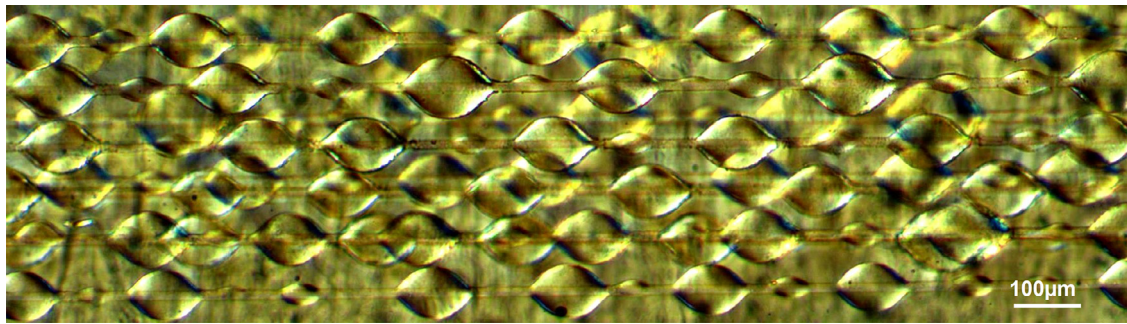


Fig. 1. A composite reinforced with beaded fibers. Epoxy beads on glass fibers embedded in epoxy matrix. Birefringence image viewed by a polarized optical microscope.

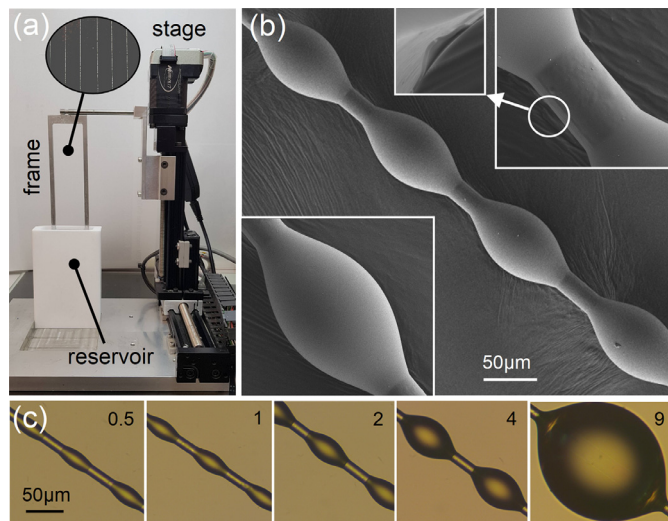


Fig. 2. Deposition of epoxy beads on glass fibers. (a) Dip coating device: a frame carrying fibers is immersed in a resin reservoir, and a controlled stage draws the frame upward at constant speed. (b) Intermittent beading spontaneously created by the Plateau-Rayleigh instability (SEM). The circled magnification shows coating of the fiber between beads, 100–200 nm thick. (c) Beads of different sizes; the numbers indicate the drawing velocity in mm/s (optical microscope).

The beads are formed on the fibers by dip coating (Fig. 2a). When drawn from a reservoir, the fibers get coated by a layer of resin, which spontaneously breaks down into almost evenly spaced drops as a result of the Plateau-Rayleigh instability (de Gennes et al., 2004). After curing, the beaded fibers (Fig. 2b) are embedded in a matrix and the composite is cured. The beads size, shape and frequency depend on the liquid coating radius (fiber radius + coating thickness) and surface tension, as described in detail in ref. (Greenfeld et al., 2018) and in the Supporting Information. Roughly, the bead radius is close to twice the coating radius, and the distance between beads (wavelength) is close to ten times the coating radius. The coating radius is determined by the drawing velocity of the fiber from the resin reservoir, making it possible to tune the beads size and frequency (Fig. 2c).

Under load, a beaded fiber composite may eventually break as a result of failure in any of its components – fiber, matrix or bead, or in any of the interfaces—fiber-matrix, fiber-bead or bead-matrix. It is therefore essential to understand the evolution of stresses in these regions under an external increasing load. Unlike a regular fiber composite, whose structure consists of just two materials and one interface, the structure of a beaded fiber composite consists of three materials and three interfaces as well as an intricate bead geometry, and therefore its analysis is significantly more challenging. Here, we focus on theoretical analysis of the elastic behavior of this complex structure, by extending the classic Cox shear lag theory (Cox, 1952) to beaded fibers. The core model is described in Section 2, whereas the detailed results and implications are provided in the subsequent sections. The results are supported by finite element analysis of a representative structure. The composite stiffness (tensile modulus) is calculated for various material combinations, bead sizes and bead shapes. The interfacial bonding stresses are also calculated, and their impact on the composite failure mode is assessed. The maximum fiber stress and interfacial bonding stresses are also calculated, and their impact on the composite strength and failure mode is assessed.

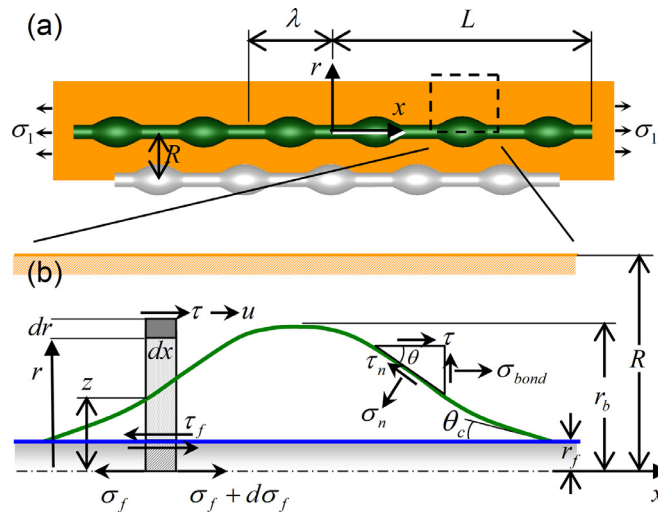


Fig. 3. Dimensions and stresses in a beaded fiber composite. See definition of parameters in the text. (a) Composite unit cell with a six-bead fiber (dark) and a neighboring fiber (faint) (b) Single bead axisymmetric profile.

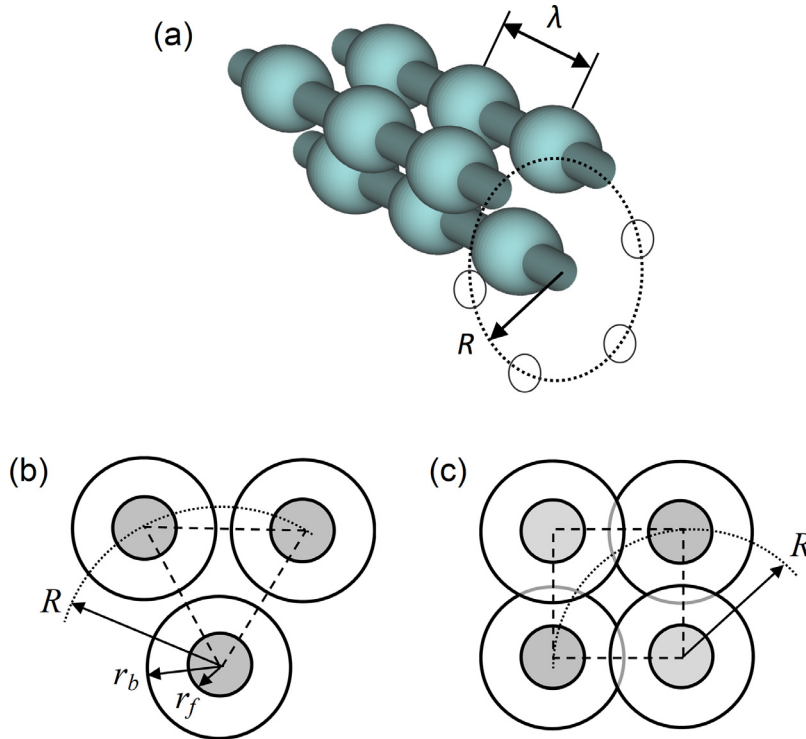


Fig. 4. Packing of beaded fibers. (a) Ring of closest neighbors. R denotes the radial distance between the centers of nearby fibers. (b) Non-staggered hexagonal packing. (c) Staggered square packing. The dashed triangle and square denote unit cells.

2. Elastic model

Consider a composite consisting of beaded fibers embedded in a matrix (Fig. 3a), subjected to longitudinal tension along the x axis. The bead contour shape, determined by surface tension of the liquid drop before curing, is described by its local radius z (Fig. 3b) for given bead peak radius r_b and contact angle θ_c with the fiber (Greenfeld et al., 2018) (see Supporting Information). The beads are assumed to be evenly dispersed along each fiber at wavelength λ , and the beaded fibers are orderly packed within the matrix with a radial distance R between the centers of nearby fibers (Fig. 4a).

Given the fiber radius r_f , the fiber volume fraction is proportional to the cross sectional area fraction of the fibers with respect to the composite unit cell

$$V_f = P_f \left(\frac{r_f}{R} \right)^2 \quad (1)$$

where P_f is the fibers packing factor, $2\pi/\sqrt{3}$ for hexagonal packing (Fig. 4b) and π for square packing (Fig. 4c) (Piggott, 2002). The maximum obtainable volume fraction V_{fmax} occurs when the beads are in contact with neighboring beads (non-staggered packing) or neighboring fibers (staggered packing) (Greenfeld et al., 2018). In non-staggered hexagonal packing, the total cross sectional area of fibers in a triangular unit cell with edge $R_{min} = 2r_b$ is that of half a fiber. As seen in Fig. 4c, in staggered square packing, the total cross sectional area of fibers in a square unit cell with edge $R_{min} = r_f + r_b$ is that of a full fiber. Thus,

$$V_{fmax} = \pi / \begin{cases} 2\sqrt{3}r_b^2/r_f^2 & \text{non-staggered hexagonal packing} \\ (1 + r_b/r_f)^2 & \text{staggered square packing} \end{cases} \quad (2)$$

We are interested in the elastic stress transfer from the matrix to the fibers through the beads, assuming perfect bonding in the three relevant interfaces: fiber-matrix, fiber-bead or bead-matrix. The model extends the known shear lag theory for beadless fiber composites (Cox, 1952; Piggott, 2002) to beaded fiber composites, and applies similar assumptions and approximations. Given the composite longitudinal stress σ_1 (Fig. 3a), the composite tensile strain ε_1 is assumed to be constant around the ring R of closest neighboring fibers. Both σ_1 and ε_1 are construed as mean values, as the arbitrary longitudinal position of beaded fibers with respect to their lateral neighbors may cause local variations. However, σ_1 and ε_1 should average over a cross section through a large number of fibers, and therefore the stresses in the bead and matrix can be modeled as axisymmetric, that is uniform at any angular position around the x axis.

Fibers longitudinal arrangement, that is the regular or random staggering of fibers with respect to their neighbors, is known to have an effect on the stiffness, strength and failure mode of unidirectional composites (Lei et al., 2012; Sun et al., 2015; Zhang et al., 2010). In beaded fibers, the relative longitudinal position of beads with respect to beads in neighboring fibers is expected to cause an additional effect. As the focus in the current study is on the stress transfer properties of beads, longitudinal arrangement considerations are not incorporated in the model, but their effects should be similar to those in beadless-fiber composites. Accordingly, the model is invariant with respect to the relative longitudinal position of neighboring fibers (so long as their beads do not interfere), and it therefore applies to both non-staggered and staggered packing of fibers and beads with the proper packing factor and maximum volume fraction applied.

Under the applied tension, an infinitesimal ring element dx (dotted region in Fig. 3b) is subject to a shear stress τ_f on its internal radius r_f (the fiber radius) and a shear stress τ on its external arbitrary radius r (refer to definitions in Fig. 3). Tensile stresses have a negligible effect on the ring static equilibrium, as the predominant stresses are in shear. Thus, the force balance between the internal and external shear forces, $2\pi r_f dx \tau_f$ and $2\pi r dx \tau$, yields

$$\tau_f = \tau \frac{r}{r_f} = G \frac{du}{dr} \frac{r}{r_f} \quad (3)$$

τ was replaced above by Hooke's law in shear, $\tau = Gdu/dr$ where G is a shear modulus, u is the longitudinal displacement at radius r (Fig. 3b), and du/dr is the shear strain at radius r (the radial displacement is negligible). The shear modulus G is a function of r , such that when r is inside the bead volume, $G = G_b$ (bead modulus), and when it is inside the matrix volume, $G = G_m$ (matrix modulus).

Separating the variables and integrating over the full radial range of the ring element from r_f to the bead local radius z (at position x) and further on to the unit cell radius R , we get

$$\int_{u_f}^{u_R} du = \tau_f r_f \int_{r_f}^R \frac{dr}{Gr} = \tau_f r_f \left(\int_{r_f}^z \frac{dr}{G_b r} + \int_z^R \frac{dr}{G_m r} \right) \quad (4)$$

where G_b was used for the first integration interval and G_m was used for the second interval. Note that the integration range is always valid as $R > z$ for all fiber packing configurations. At fiber sections without beads $z = r_f$ and thus the first integral vanishes. Eq. (4) marks the departure of the model from the Cox model for beadless fibers, in which the integration is directly from r_f to R with a single shear modulus, G_m .

We perform the integration in Eq. (4)

$$u_R - u_f = \frac{2\tau_f r_f}{E_f n^2} \quad (5)$$

where we introduced the dimensionless function

$$n^2 = \frac{2G_m}{E_f} \left[\frac{G_m}{G_b} \ln \left(\frac{z}{r_f} \right) + \ln \left(\frac{R}{z} \right) \right]^{-1} \quad (6)$$

As the beads profile z is a periodic function of x with period λ , n is also a periodic function of x with period λ . n can be rewritten by expressing R in terms of V_f and P_f using Eq. (1):

$$n^2 = \frac{2G_m}{E_f} \left[\frac{1}{2} \ln \left(\frac{P_f}{V_f} \right) - \left(1 - \frac{G_m}{G_b} \right) \ln \left(\frac{z}{r_f} \right) \right]^{-1} \quad (7)$$

The reaction shear force on a fiber element dx (hatched region in Fig. 3b), $2\pi r_f dx \tau_f$, induces a change $d\sigma_f$ in the fiber stress and a longitudinal net force $\pi r_f^2 d\sigma_f$. These forces are in equilibrium so that

$$\tau_f = -\frac{r_f}{2} \frac{d\sigma_f}{dx} \quad (8)$$

The negative sign means that $d\sigma_f$ is negative, in other words the fiber stress changes in the opposite trend of τ_f . Substituting τ_f into Eq. (5) we get

$$u_R - u_f = -\frac{r_f^2}{E_f n^2} \frac{d\sigma_f}{dx} \quad (9)$$

Differentiating with respect to x

$$\frac{du_R}{dx} - \frac{du_f}{dx} = -\frac{1}{E_f} \frac{d}{dx} \left(\frac{r_f^2}{n^2} \frac{d\sigma_f}{dx} \right) \quad (10)$$

Substituting $du_R/dx = \varepsilon_1$ (the composite strain at radius R) and $du_f/dx = \sigma_f/E_f$ (the fiber strain, given its tensile modulus E_f) and rearranging, we obtain the differential equation:

$$\frac{d}{dx} \left(\frac{r_f^2}{n^2} \frac{d\sigma_f}{dx} \right) = \sigma_f - \varepsilon_1 E_f \quad (11)$$

The boundary conditions are $\sigma_f(-L) = 0$ and $\sigma_f(L) = 0$ as the fiber stress at its ends is zero (the fiber end-face bonding is neglected). Alternatively, the second boundary condition can be set as $d\sigma_f(0)/dx = 0$ at the fiber center, because, due to symmetry, τ_f changes direction (sign) at that point and therefore tends to zero (Eq. (8)). Once σ_f is obtained by solving Eq. (11) for given beads profile z and elastic constants, τ_f can be calculated from Eq. (8). Note that the differential Eq. (11) becomes independent of the fiber radius if the length variables x , z and L are normalized by r_f . The equation reverts to the classic Cox shear lag model for beadless fibers when the bead and matrix are of the same material ($G_m = G_b$ and hence $n^2 = n_{\text{cox}}^2 = 4G_m/[E_f \ln(P_f/V_f)]$).

Eq. (11), with its boundary conditions and the function n (Eq. (7)), encapsulates all the parameters involved in the model. These include the applied external strain ε_1 , the elastic constants of the structural components E_f , G_m and G_b , the fibers volume fraction and packing factor V_f and P_f , the fiber geometry r_f and L , and the beads contour shape (profile) z . The model retains the generality of the function z , which can describe any desired beads profile, even with irregular shapes and repetitions. However, in the current study we use Plateau-Rayleigh beading, in which, once the bead radius r_b and contact angle θ_c are given, the beads shape and wavelength λ are determined and z is fully defined (see calculation and plot in Supporting Information). The number of beads in a fiber, N , is readily extracted from the fiber length $2L$ and the distance between beads λ , typically $N = \lceil 2L/\lambda \rceil$.

Eq. (11) is a second order linear ordinary differential equation, whose coefficient r_f^2/n^2 is an even periodic function of x with period λ . The particular solution of this equation is $\sigma_f = \varepsilon_1 E_f$. The homogenous part of the equation, seen when the term $\varepsilon_1 E_f$ is omitted, is known as Hill's equation (Hill, 1877). Hill investigated this type of equation in 1877 to assess the periodic disturbance induced by the sun's gravity on the lunar perigee, and it appears often in models of periodic phenomena in engineering and physics (Magnus and Winkler, 1979). However, an explicit general solution of this equation is not available, and therefore analytic approximations and/or numerical solutions must be used. The modeling results and implications presented in the following sections were obtained by numerical calculations, but, for the sake of better physical insight, analytic approximations are provided as well.

3. Fiber stresses

Examples of the fiber tensile and interfacial stresses for epoxy matrix reinforced by high-stiffness carbon fibers are depicted in Fig. 5 for fibers with different length and bead numbers, and are compared with the shear lag theory for beadless fibers. The bead stiffness plays an important role in the stiffness of a beaded fiber composite. To demonstrate its potential, the bead stiffness was chosen in that example as five times higher than that of the matrix. Apparently, that effect vanishes when the bead has the same stiffness as the matrix. The beads anchoring is seen in the elevated interfacial stress at the bead sites, especially at beads close to the fiber ends, and is also reflected in the overall higher fiber stress compared to beadless fibers.

More examples are shown in Fig. 6, which demonstrates the effect of bead (a) and fiber (b) stiffness in 8-beaded fibers. As seen, higher bead stiffness increases the shear and fiber stresses, reflecting a better stress transfer from the matrix. The

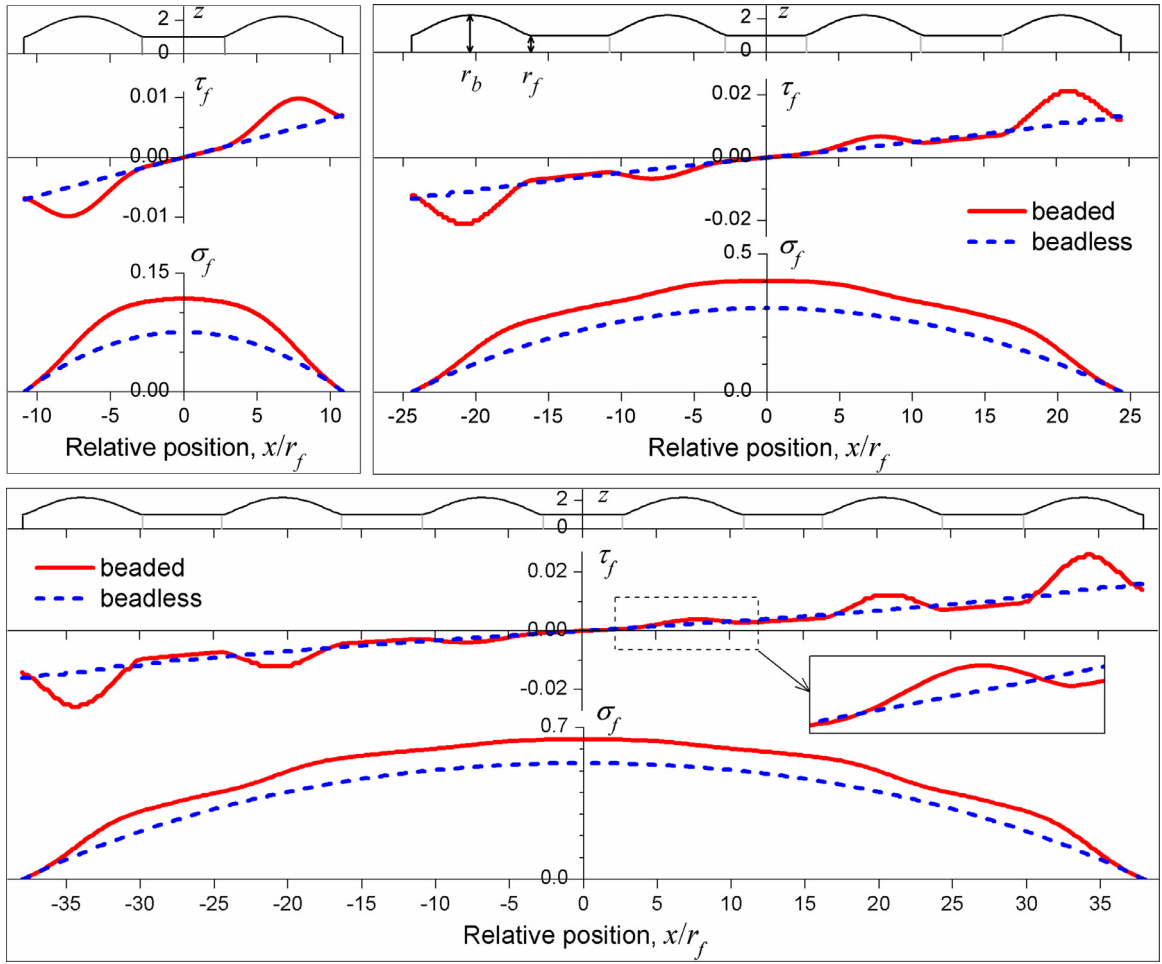


Fig. 5. Elastic stresses in beaded fiber composites. The fiber tensile stress σ_f and interfacial stress τ_f , are depicted versus the relative position along the fiber, x/r_f , for beaded fibers with for 2, 4 and 6 beads and for beadless fibers (bead-to-matrix tensile moduli ratio $E_b/E_m = 5$ and 1, respectively). Both stresses are normalized by $\varepsilon_1 E_f$, where ε_1 is the composite strain and E_f is the fiber tensile modulus. The fiber volume fraction in the composite is $V_f = 0.3$. The beads profile z is shown at the top of each case. The beads relative radius is $r_b/r_f = 2.22$, their contact angle with the fiber is $\theta_c = 15^\circ$, and their relative wavelength is $\lambda/r_f = 13.57$. The fiber, bead and matrix tensile moduli are 750 GPa, 8 GPa and 1.6 GPa, respectively, with Poisson ratio 0.33 for both bead and matrix .

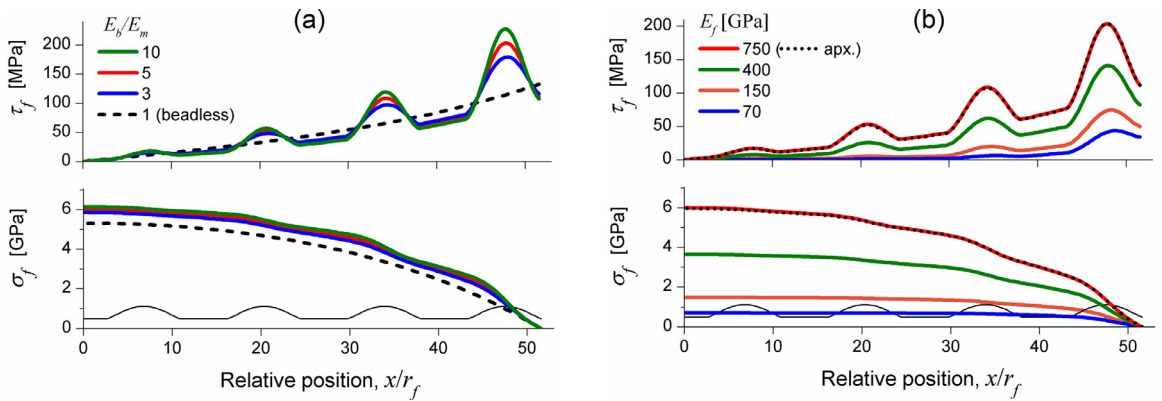


Fig. 6. Elastic stresses in beaded fiber composites. For fibers with 8 beads each (only the right half is shown), subjected to composite strain $\varepsilon_1 = 0.01$. The parameters in the red curves are as in Fig. 5, with modulation of (a) the bead relative modulus E_b/E_m , and (b) the fiber modulus E_f . The dotted lines are analytic approximations by Eqs. (16) and (17).

composite is elastic, and therefore the stresses are linearly dependent on the composite strain ε_1 and can be interpolated or extrapolated for different strains. In these examples the outermost beads are flush with the fiber ends, but conformations in which the fiber protrudes further from the outermost beads can also be described, by setting a desired fiber length L (for example an even multiple of λ) in the boundary conditions.

The fiber tensile and shear stresses can both be described as a superposition of a reference stress, similar in shape to that of beadless fibers but of higher magnitude, and a stress perturbation that grows toward the fiber ends and is predominant at bead sites. Using this approach, approximate analytic expressions can be derived for the stresses. The reference stress, or zero-order solution (indicated by the subscript 0), is obtained by setting an effective (or mean) constant value of n , denoted by \bar{n} , in the differential equation of σ_f (Eq. (11))

$$\frac{d^2\sigma_{f0}}{dx^2} = \frac{\bar{n}^2}{r_f^2}(\sigma_{f0} - \varepsilon_1 E_f) \quad (12)$$

where \bar{n} is defined by the mean of n from Eq. (7)

$$\bar{n} = \frac{1}{\lambda} \int_0^\lambda n dx \cong \frac{1}{2}(n_f + n_b) \quad (13)$$

The Plateau-Rayleigh beading generally maintains a constant ratio between the bead diameter and the wavelength (Greenfeld et al., 2018). Consequently, \bar{n} could be approximated in the above equation by the average between the values of n at the peak (max radius) of a bead, $n_b = n(z = r_b)$, and at its bottom, $n_f = n(z = r_f) = n_{\text{cox}}$.

The solution of Eq. (12) is of the form $\sigma_f = \varepsilon_1 E_f + A \sinh(\bar{n}x/r_f) + B \cosh(\bar{n}x/r_f)$, where, using the boundary conditions $\sigma_{f0}(-L) = \sigma_{f0}(L) = 0$, the constants are $A = 0$ and $B = -\varepsilon_1 E_f / \cosh(\bar{n}L/r_f)$, yielding the zero-order fiber tensile stress

$$\sigma_{f0} = \varepsilon_1 E_f \left[1 - \frac{\cosh(\bar{n}x/r_f)}{\cosh(\bar{n}L/r_f)} \right] \quad (14)$$

Substituting in Eq. (8), the zero-order fiber shear stress is

$$\tau_{f0} = \frac{1}{2} \bar{n} \varepsilon_1 E_f \frac{\sinh(\bar{n}x/r_f)}{\cosh(\bar{n}L/r_f)} \quad (15)$$

Both results resemble those of beadless fibers (Piggott, 2002), except that n_{cox} is replaced by \bar{n} (Eq. 13).

More accurate first-order approximations are necessary, especially for the shear stress whose perturbations are large. The rationale for the following approximations is explained in the Supporting Information. We use the function $n^2/\bar{n}^2 - 1$ to describe the periodic relative deviation of n from its mean value \bar{n} . The first-order approximation for the shear stress is given by

$$\tau_{f\text{apx}} \cong \tau_{f0} + \tau_{f0} \left(\frac{n^2}{\bar{n}^2} - 1 \right) \cong \tau_{f0} \frac{n^2}{\bar{n}^2} \quad (16)$$

The term τ_{f0} represents the reference shear stress, whereas the term $\tau_{f0}(n^2/\bar{n}^2 - 1)$ describes the perturbation. Integrating $\tau_{f\text{apx}}$ (Eq. 8) from the fiber end toward its center, the first-order approximation for the tensile stress is given by

$$\sigma_{f\text{apx}} \cong -\frac{2}{r_f} \int_L^x \tau_{f\text{apx}} dx \cong \sigma_{f0} - \frac{2}{r_f} \int_L^x \tau_{f0} \left(\frac{n^2}{\bar{n}^2} - 1 \right) dx \quad (17)$$

The term σ_{f0} represents the reference tensile stress, whereas the second term describes the perturbation. The maximum fiber stress at its center is $\sigma_{f\text{max}} = \sigma_{f\text{apx}}(0) = \sigma_{f0}(0)$. These approximations are depicted in Fig. 6b (dotted curves) for the case $E_f = 750\text{GPa}$ with $\bar{n} = 0.045$, demonstrating excellent fitting accuracy ($R^2 > 0.999$, initial guess $\bar{n} = 0.046$ from Eq. (13)).

4. Finite element model

The fiber tensile and interfacial stresses obtained by the model were compared to finite element analysis (FEA) of a four-beaded fiber embedded in a matrix. The FEA model is described in Fig. 7, showing the right side of the fiber in an axisymmetric structure. The FEA adopts the same loading approximation as in Cox model, by applying a uniform composite strain ε_1 at the ring R . Thus, the average effect of the closest neighboring fibers is emulated, and the FEA unit cell is simplified to a single fiber. The FEA helps validate the stress fluctuations induced by the beads predicted by the elastic model, as well as the peak stresses. The FEA also yields the stress concentrations and radial and circumferential stresses, which are absent from the analytic model.

The elastic model is generally corroborated by the FEA, as demonstrated in Fig. 8 for a four-beaded fiber composite. It is seen that the analytic calculation of the fiber tensile and shear stresses, σ_f and τ_f , fits the FEA reasonably well. Similar fit is seen also for the bead and matrix tensile stresses (presented in Fig. 11). These results indicate that, although the elastic model neglects the radial and circumferential stresses, the tensile and shear stresses are modeled appropriately. Thus, the stiffness calculations (in Section 5) based on these stresses should be valid. The elastic model does not show the stress

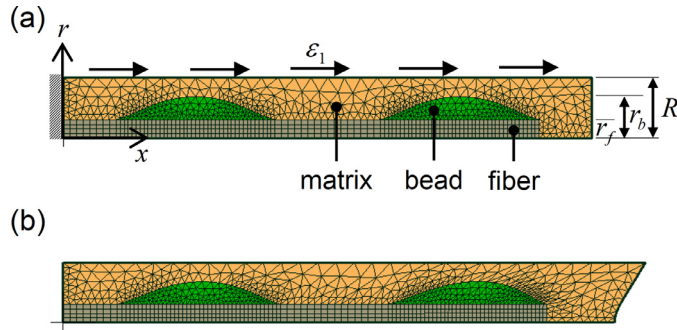


Fig. 7. Finite element model of a beaded fiber composite unit cell. Run on Mecway FEA software. The model is shown before (a) and after (b) loading (with displacement magnification $\times 30$). The parameters are as in Fig. 5. The model is 2D axisymmetric around the x axis, showing the right side of a four-beaded fiber embedded in a matrix. The structure is constrained in the x direction at $x = 0$ and in the r direction at $r = 0$. The load is applied by imposing a uniform strain $\varepsilon_1 = 0.0042$ on the matrix external radius R (equivalent to overall elongation of $1\ \mu\text{m}$). The model dimensions are: $r_f = 9\ \mu\text{m}$, $r_b = 20\ \mu\text{m}$, $R = 29.1\ \mu\text{m}$ and length $244.2\ \mu\text{m}$ ($V_f = 0.3$).

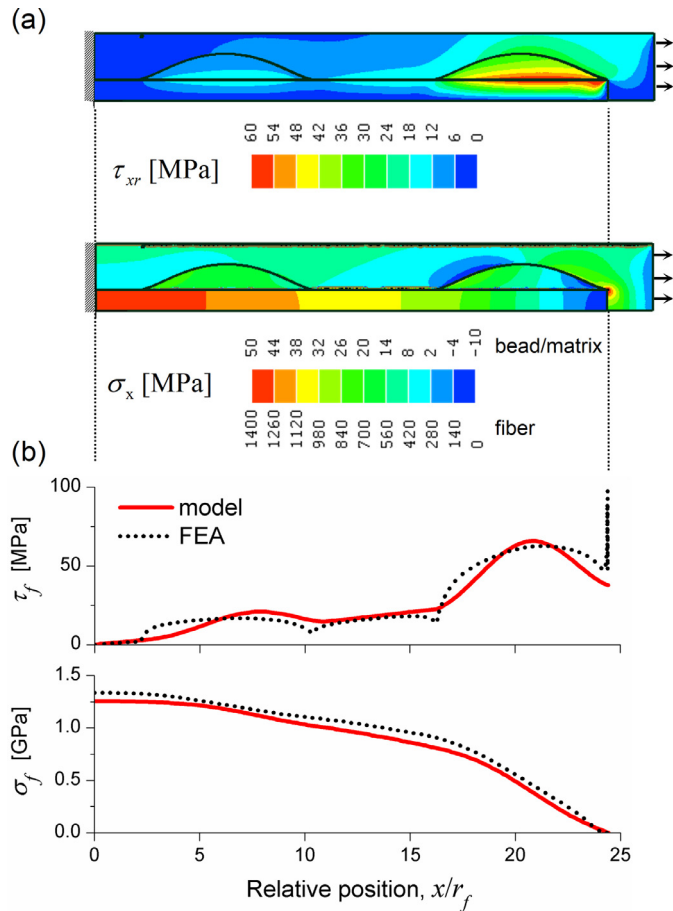


Fig. 8. Finite element analysis (FEA) of the elastic stresses. The model is described in Fig. 7. (a) Stress maps in shear (τ_{xr}) and tension (σ_x). (b) The fiber interfacial stress τ_f and tensile stress σ_f , depicted versus the relative position along the fiber, x/r_f , compared to the model described by Eq. (11).

concentrations in tension and shear, which appear in the FEA at the fiber end, a known occurrence in fiber composites (Piggott, 2002). To obtain the details of these stress concentrations, the FEA mesh had to be refined in that region to a resolution of about $0.1\ \mu\text{m}$ per element.

5. Composite stiffness

The higher fiber stress in a beaded fiber composite, as well as the higher bead stiffness (with respect to the matrix), contribute to higher composite tensile modulus. A transverse cross section through the composite will cut through a large number of parallel fibers and beads which are arbitrarily dispersed in the longitudinal direction. Thus, the overall longitudinal stress contributed by the fibers is their average stress multiplied by their area fraction (that is, volume fraction). Similarly, the overall longitudinal stress contributed by the beads will be their average stress multiplied by their volume fraction. Hence, we can use the following rule of averages to obtain the mean composite stress in the longitudinal direction (direction 1)

$$\sigma_1 = V_f \bar{\sigma}_f + V_b \bar{\sigma}_b + V_m \bar{\sigma}_m \quad (18)$$

where $\bar{\sigma}$ denotes average stress and V denotes volume fraction. The fiber volume fraction V_f depends on the fibers packing conformation (Eq. (1)), and its maximal value is bounded by the ratio between the bead and fiber radii (Eq. 2). The fiber average stress is obtained by integrating σ_f (solution of Eq. (11)) from the fiber center to its end

$$\bar{\sigma}_f = \frac{1}{L} \int_0^L \sigma_f dx \quad (19)$$

Given the beads profile z (the bead local radius) on a fiber of given length, the ratio between the beads and fiber volumes is known. The bead volume fraction can be calculated by multiplying V_f by that ratio:

$$V_b = V_f \frac{v_b}{\pi r_f^2 L}, \text{ where } v_b = \pi \int_0^L (z^2 - r_f^2) dx \quad (20)$$

where v_b is the volume of all the beads from the fiber center to its end. To obtain the average bead stress, we integrate Eq. (4) from r_f to an arbitrary radial position r inside the bead

$$u_r - u_f = \frac{\tau_f r_f \ln(r/r_f)}{G_b} \quad (21)$$

Differentiating with respect to x , the longitudinal tensile strain and stress inside the bead are

$$\varepsilon_b = \frac{\sigma_f}{E_f} + \frac{r_f \ln(r/r_f)}{G_b} \frac{d\tau_f}{dx}, \quad \sigma_b = \varepsilon_b E_b \quad (22)$$

where the following substitutions were made: $du_r/dx = \varepsilon_b$ and $du_f/dx = \sigma_f/E_f$. The volume of an infinitesimal ring element $drdx$ (the gray region in Fig. 3b) is $2\pi r dr dx$. The bead average stress is calculated by integrating the bead stress in that ring element throughout the entire volume of beads on a fiber, v_b (Eq. 20), from the fiber center to its end

$$\bar{\sigma}_b = \frac{2\pi}{v_b} \int_0^L \int_{r_f}^z \sigma_b r dr dx \quad (23)$$

In words, the bead average stress is the summation, over the entire beads volume on half a fiber, of the stress at each volume element weighted by its volume fraction. Note that although the bead is generally under longitudinal tension ($\sigma_b > 0$), its stress can locally turn negative ($\sigma_b < 0$) close to the fiber ends (to be discussed later), and the contribution of such local compression to the bead average stress would be negative.

The matrix volume fraction is $V_m = 1 - V_f - V_b$, and its average stress can be calculated in the same manner as for the bead, except that the integration range in Eq. (4) is from r_f to an arbitrary radial position r inside the matrix:

$$\varepsilon_m = \frac{\sigma_f}{E_f} + \frac{2r_f}{E_f} \frac{d}{dx} \left(\frac{\tau_f}{n_r^2} \right), \quad \sigma_m = \varepsilon_m E_m \quad (24)$$

where $n_r = n(R=r)$ is obtained by replacing R by r in Eq. (6). The matrix average stress can be calculated by integrating the stress throughout the matrix entire volume, but, as the matrix strain is on average the same as that of the composite, we approximate the average stress by $\bar{\sigma}_m = \varepsilon_1 E_m$. In Eqs. (22) and (24), τ_f and $d\tau_f/dx$ can be exchanged by $d\sigma_f/dx$ and $d^2\sigma_f/dx^2$, respectively, obtained from Eq. (8) and its derivative.

Finally, the composite modulus is

$$E_1 = \frac{\sigma_1}{\varepsilon_1} = \frac{V_f \bar{\sigma}_f + V_b \bar{\sigma}_b + V_m \bar{\sigma}_m}{\varepsilon_1} \quad (25)$$

The contributions of the fibers and beads to the modulus of this composite are depicted in Fig. 9 for epoxy reinforced by glass (a) and carbon (b) fibers. The higher fiber average stress induced by the beads is reflected in the higher fiber contribution (blue ▲ curve) compared to beadless reinforcement (dashed curve). This improvement is predominant in shorter fibers with fewer beads, and is higher for stiffer fibers (Fig. 9b). The beads themselves, which are five times stiffer than the

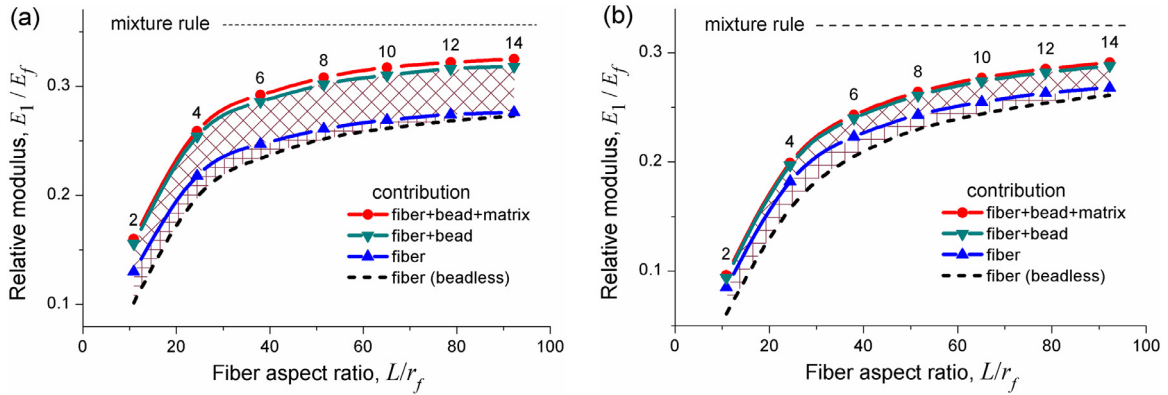


Fig. 9. Contributions of the fibers and beads to the composite modulus. The composite modulus E_1 , normalized by the fiber modulus E_f , is shown in the topmost graph (●) versus the fiber aspect ratio, L/r_f . The number of beads per fiber (from 2 to 14) is indicated, and the connecting curves reflect averaging of their statistical variation. The lower patterned region indicates the improvement in fiber contribution with respect to a beadless reinforcement. The upper patterned region indicates the contribution of the beads themselves. The fiber volume fraction is $V_f = 0.3$. The beads relative radius is $r_b/r_f = 2.22$ and their contact angle with the fiber is $\theta_c = 15^\circ$. The fibers tensile modulus is 70 GPa (a) and 150 GPa (b), and the beads and matrix tensile moduli are 8 GPa and 1.6 GPa, respectively, with Poisson ratio 0.33 for both.

matrix in this example, contribute furthermore to the composite modulus. The upper limit of the composite stiffness is set by a plain mixture rule

$$E_{1\max} = V_f E_f + V_b E_b + V_m E_m \quad (26)$$

indicated in Fig. 9 for compact packing (staggered square packing, Eq. (2)). The volume fractions of the fibers, beads and matrix in this example are 0.3, 0.44 and 0.26, respectively.

The effects of material properties, beads shape and beads frequency on the composite modulus are depicted in Fig. 10, in comparison with the modulus of beadless composites. Generally, the modulus improvement is higher in shorter fibers and tends to gradually decrease as the fibers get longer and with more beads. It is also seen that the modulus improvement increases with increasing fiber modulus (a), bead modulus (b), and bead radius (c), and with decreasing contact angle (d). The bead stiffness is a dominant parameter in that it induces a higher average stress in the fibers, as well as contributes its own stiffness to the structure. Also dominant is the bead size, although a large bead radius limits the maximum possible fiber volume fraction. Note that a larger bead radius is coupled with a longer distance between beads (Fig. 10c). The effect of fiber modulus is not considerable, even though the moduli range from 70 GPa (glass fibers) to 750 GPa (high stiffness carbon fibers). The effect of contact angle is not considerable either, and small angles are favored because they result in longer beads.

Using Eq. (25) with the zero-order analytic approximations for the fiber stress σ_{f0} (Eq. 14) and the shear stress τ_{f0} (Eq. 15), the composite stiffness can be assessed by

$$E_{1\text{apx}} \cong V_f E_f \left[1 - \frac{\tanh(\bar{n}L/r_f)}{\bar{n}L/r_f} \right] + V_b E_b \left[1 - \frac{\tanh(\bar{n}L/r_f)}{\bar{n}L/r_f} K \right] + V_m E_m \quad (27)$$

The factor K is typically between 0 and 1, and is close to 1 for low values of G_m/G_b . The detailed calculation is presented in the Supporting Information. When the term $\bar{n}L/r_f \gg 1$, this equation converges to the mixture rule of Eq. (26). The modulus analytic approximation is depicted in Fig. 10c (dotted curve) for the case $r_b/r_f = 2.2$ with $\bar{n} = 0.146$, demonstrating excellent fitting accuracy (initial guess $\bar{n} = 0.146$ from Eq. (13)).

To account for fibers misorientation effects as well as for randomly oriented fibers, Eq. (27) can be rewritten as $E_{1\text{apx}} \cong \chi_{1f} \chi_{2f} V_f E_f + \chi_{1b} \chi_{2b} V_b E_b + V_m E_m$, where χ_{1f} and χ_{1b} are the fibers and beads orientation factors, and χ_{2f} and χ_{2b} are the factors in brackets in Eq. (27). The same approach as for beadless fibers (Piggott, 2002) can be applied to beaded fibers: the composite is envisioned as consisting of an infinite number of hypothetic structural components, each containing unidirectional beaded fibers with known orientation, and the overall effect is obtained by integrating over all orientations. The stress fluctuations along beaded fibers average over a large number of fibers in a cross section, and therefore the fibers orientation factor is likely the same as in beadless fibers. Furthermore, as the beads are oriented together with their hosting fibers, their misorientation factor should be the same as that of the fibers. Thus, $\chi_1 = \chi_{1f} = \chi_{1b}$, where χ_1 is the misorientation factor of beadless fibers. The value of χ_1 is 1 for unidirectional fibers, 3/8 for fibers randomly oriented in two dimensions (in laminates), and 1/5 for fibers randomly oriented in three dimensions (Piggott, 2002).

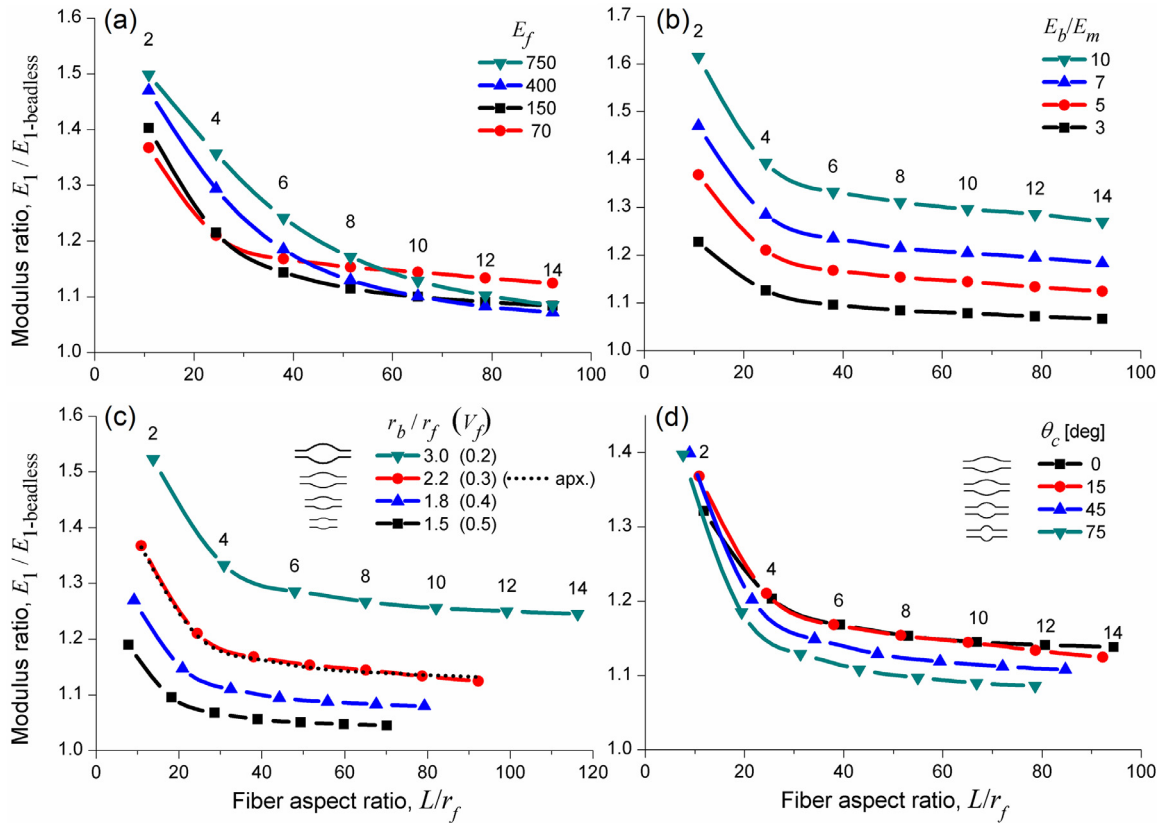


Fig. 10. Effects of material properties and beads shape on the composite modulus. The composite modulus E_1 , normalized by the modulus of a beadless fiber composite, is depicted versus the fiber aspect ratio, L/r_f . The number of beads per fiber (from 2 to 14) is indicated, and the connecting curves reflect averaging of their statistical variation. The nominal parameters (●) are as in Fig. 9a, with modulation of the following parameters: (a) fiber tensile modulus E_f , (b) bead tensile modulus with respect to matrix E_b/E_m , (c) bead relative radius r_b/r_f and corresponding maximal fiber volume fraction $V_f = V_{f_{\max}}$ (Eq. (2)); the dotted line is analytic approximation by Eq. (27), and (d) bead-fiber contact angle θ_c .

6. Interfacial stresses

The stresses close to the bead-matrix interface determine the stresses acting on the interfacial bonding. The shear stress close to the bead surface is obtained from Eq. (3) by substituting the local bead radius, $r = z$:

$$\tau = \frac{r_f}{z} \tau_f \quad (28)$$

Similarly, the bead tensile strain and stress close to its surface are obtained from Eq. (22)

$$\varepsilon_b = \frac{\sigma_f}{E_f} + \frac{r_f \ln(z/r_f)}{G_b} \frac{d\tau_f}{dx}, \quad \sigma_b = \varepsilon_b E_b \quad (29)$$

and the matrix tensile strain and stress close to the bead surface are obtained from Eq. (24)

$$\varepsilon_m = \varepsilon_b - \frac{r_f}{G_m} \left(1 - \frac{G_m}{G_b}\right) \frac{dz/dx}{z} \tau_f, \quad \sigma_m = \varepsilon_m E_m \quad (30)$$

When the bead and matrix are of the same material ($G_m = G_b$, $E_m = E_b$), the tensile stresses from both sides of the bead surface are equal ($\sigma_m = \sigma_b$). In the above equations, τ_f and $d\tau_f/dx$ can be exchanged by $d\sigma_f/dx$ and $d^2\sigma_f/dx^2$, respectively, obtained from Eq. (8) and its derivative.

The tensile and shear stresses close to the bead surface are depicted in Fig. 11 for epoxy reinforced by high stiffness carbon fibers (a) and glass fibers (b), and compare well with the FEA. The trends of the tensile stresses are opposite in the bead and matrix, that is, typically, when one is rising the other is declining. This is particularly visible in the case of the high stiffness carbon fibers (Fig. 11a) in the bead close to the fiber end: on its right side, the bead is under compression whereas the matrix is under tension; on its left side, the bead is under tension whereas the matrix is under compression.

In the case of the glass fibers (Fig. 11b), the bead stress is much higher than the matrix stress, and the stress rises toward the fiber center. So, the lower stiffness fiber (glass) elongates more and thus relieves some of the tension in the matrix, but

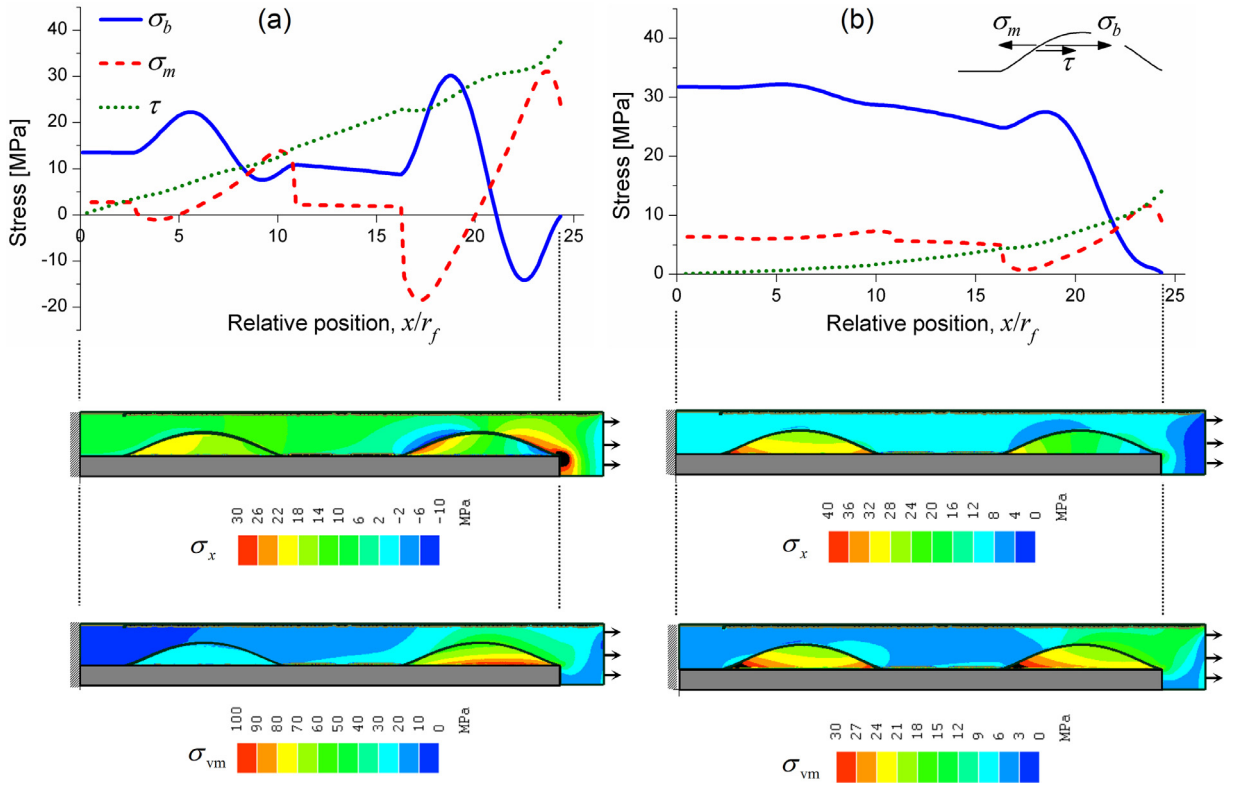


Fig. 11. Bead and matrix stresses. The bead and matrix longitudinal tensile stresses, σ_b and σ_m , and the shear stress, τ , close to the bead surface, are depicted versus the relative position along the fiber, x/r_f , for fibers with 4 beads each (only the right half is shown). The parameters are as in Fig. 5. The composite strain is $\varepsilon_1 = 0.0042$. The corresponding FEA stress maps of the longitudinal stress, σ_x , and von Mises stress, σ_{vm} , are shown below the plots. The fiber modulus E_f is (a) 750 GPa (high stiffness carbon), and (b) 70 GPa (glass).

at the same time transfers higher strain and stress to the bead. Note that the bead tensile stress in the gaps between beads is not zero, as might be expected, because the solution of the model accounts for an infinitesimal layer of bead material on the fiber ($z \rightarrow r_f$). Such nanoscale layer about 100–200 nm thick, seen in the magnified inset in Fig. 2b, was indeed observed experimentally (Greenfeld et al., 2018).

The bead-matrix interface includes a thin bonding layer that holds the bead and matrix together. Given the layer stiffness constants, E_{bond} and G_{bond} , the longitudinal strain in the bonding layer, ε_{bond} , is given by Eq. (30) with G_m replaced by G_{bond} , and the longitudinal stress is therefore $\sigma_{bond} = \varepsilon_{bond} E_{bond}$. The shear stress in the bonding layer remains τ (Eq. 28), as it does not depend on the layer stiffness. We neglected here the effect of the bonding layer on the model, as the integration in Eq. (4) should incorporate an additional integration interval across the bonding layer, and would consequently add a term to n in Eqs. (6) and (7). However, the bonding layer is infinitesimally thin, and hence this effect is negligible.

We are interested in the bonding layer in-plane and normal stresses – the tangential (shear) stress τ_n and the normal (tensile) stress σ_n , illustrated in Fig. 12a. Considering a triangular infinitesimal element in the bonding layer (Fig. 3b), these bonding stresses are at equilibrium with the stresses acting in the directions of the main axes, τ and σ_{bond} . The transformation angle is determined by the bead local slope

$$\theta = \tan^{-1}(dz/dx) \quad (31)$$

positive when the slope is rising and negative when it is declining. Projecting τ and σ_{bond} on the normal and tangential directions, and balancing the forces in each direction (Timoshenko and Goodier, 1970), we obtain

$$\begin{aligned} \sigma_n &= \sigma_{bond} \sin^2 \theta - \tau \sin 2\theta \\ \tau_n &= -\frac{1}{2} \sigma_{bond} \sin 2\theta + \tau (\cos^2 \theta - \sin^2 \theta) \end{aligned} \quad (32)$$

The radial tensile stress was neglected as the predominant stresses are longitudinal.

The bead-matrix bonding stresses are depicted in Fig. 12 for two cases of bead stiffness: same stiffness as the matrix (a), and higher stiffness than the matrix (b). We assume that the bonding layer is part of the matrix, and therefore has the same elastic properties and longitudinal stress as the matrix ($\sigma_{bond} = \sigma_m$). This assumption is compared to a case where the bonding layer is five times less stiff than the matrix (thin curves), for example when coating is applied. It is seen that τ_n is

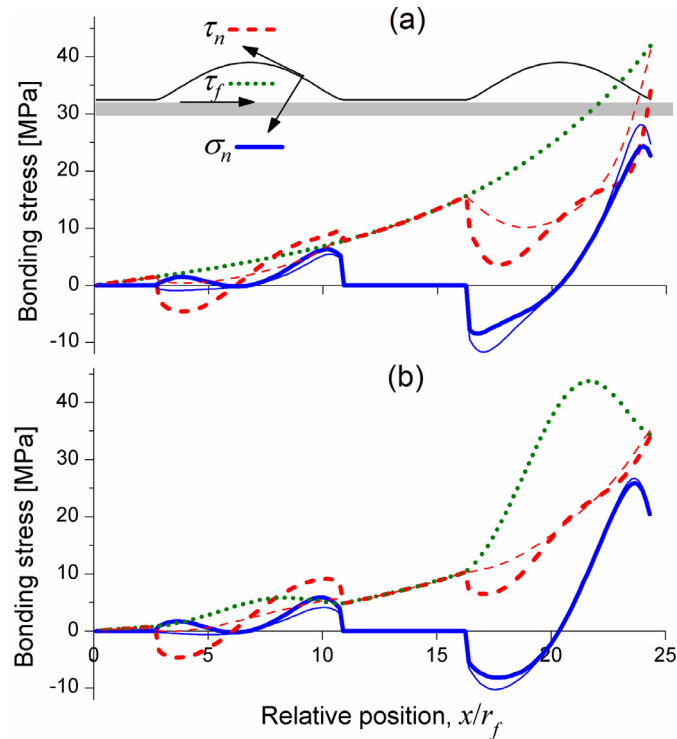


Fig. 12. Bead interfacial bonding stresses. The bead-fiber interfacial stress, τ_f , and the bead-matrix normal and tangential interfacial stresses, σ_n and τ_n , are depicted versus the relative position along the fiber, x/r_f , for fibers with 4 beads each (only the right half is shown). The elastic properties of the bead-matrix bonding layer are (i) same as the matrix ($E_{bond} = E_m$, thick curves), and (ii) five times weaker than the matrix ($E_{bond} = E_m/5$, thin curves). The parameters are as in Fig. 5 except when noted otherwise. The composite strain is $\varepsilon_1 = 0.01$ and the fiber modulus E_f is 70 GPa (glass). The bead relative modulus E_b/E_m is (a) 1, that is same material as the matrix, and (b) 5.

generally lower than τ_f or about the same. However, the magnitude of the normal bonding stress σ_n is significant, particularly when it acts in tension. So, the bead-matrix bonding interface simultaneously bears both shear and normal tension. By comparison, the fiber interface does not carry a stress normal to its bonding layer. Note that σ_n is fairly insensitive to the bead stiffness: a change from same stiffness as the matrix (Fig. 12a) to five times higher (Fig. 12b) has a rather minor effect. Also, a change from same bonding stiffness as the matrix to five times weaker has a rather minor effect.

7. Composite strength and failure modes

The stresses that develop in the fiber, bead, matrix and bonding interfaces, and the corresponding strength of each of these structural components, determine where failure could initiate and consequently the composite ultimate strength. For example, as seen in Fig. 12, the bead-matrix bonding layer bears both shear and tensile stresses, whose combination might exceed the interfacial strength prior to fiber-bead debonding. The combined effect of the tensile and shear stresses in the beads and matrix is best described (for ductile materials) by the von Mises stress—see FEA examples at the bottom of Fig. 11.

The maximum fiber stress occurs at its center ($x = 0$). Using Eq. (14), the maximum fiber tensile stress can be approximated by

$$\sigma_{fmax} \cong \sigma_{f0}(0) \cong \varepsilon_1 E_f \left[1 - 1 / \cosh(\bar{n}L/r_f) \right] \quad (33)$$

where the effective parameter \bar{n} is defined by Eq. (13).

The bead-fiber interfacial stresses comprise the bead shear and tensile stresses at the boundary layer. The maximum bead shear stress has a peak that nearly coincides with the highest point of the bead closest to the fiber end (Fig. 6), at longitudinal position

$$x_b \cong (N - 1) \frac{\lambda}{2} \quad (34)$$

where N is the number of beads on the fiber. Using Eq. (16), the maximum bead shear stress at the boundary layer can be approximated by

$$\tau_{b \max} \cong \tau_{f \text{apx}}(x_b) \cong \frac{1}{2} \bar{n} \varepsilon_1 E_f \frac{\sinh(\bar{n} x_b / r_f) n_b^2}{\cosh(\bar{n} L / r_f) \bar{n}^2} \quad (35)$$

where $n_b = n(x_b)$ is the value of n at the bead peak (max radius, $z = r_b$). At that location, the tensile stress in the bead is approximated by combining Eqs. (14) and (22) with $r = r_f$

$$\sigma_b \cong \sigma_{f0}(x_b) \frac{E_b}{E_f} \cong \varepsilon_1 E_b \left[1 - \frac{\cosh(\bar{n} x_b / r_f)}{\cosh(\bar{n} L / r_f)} \right] \quad (36)$$

To evaluate the combined bead-fiber bonding stress that may lead to failure, we calculate the maximum von Mises stress at that interface

$$\sigma_{b \text{vm}} \cong \sqrt{\sigma_b^2 + 3\tau_{b \max}^2} \quad (37)$$

The contribution of the tensile component σ_b is relatively small because it tends to zero toward the fiber end.

The matrix-bead interfacial stresses comprise the matrix shear and tensile stresses at the boundary layer. The maximum matrix shear stress at the boundary layer (Eqs. (16) and (28), Fig. 11) occurs at the fiber end, where $x = L$ and $z = r_f$

$$\tau_{m \max} \cong \tau_{f \text{apx}}(L) \cong \frac{1}{2} \bar{n} \varepsilon_1 E_f \tanh(\bar{n} L / r_f) \frac{n_f^2}{\bar{n}^2} \quad (38)$$

where $n_f = n(L)$ is the value of n at the fiber end ($z = r_f$). The corresponding tensile stress at that location is approximated by Eq. (30) with $\sigma_f = 0$, $z = r_f$ and $\dot{z} = -\tan(\theta_c)$

$$\sigma_m \cong k \tau_{m \max}, \quad k = 2(1 + \nu_m) \left(1 - \frac{G_m}{G_b} \right) \tan(\theta_c) \quad (39)$$

where $E_m/G_m = 2(1 + \nu_m)$ and ν_m is the matrix Poisson's ratio. To evaluate the combined matrix-bead bonding stress that may lead to failure, the maximum von Mises stress at that interface is

$$\sigma_{m \text{vm}} = \sqrt{\sigma_m^2 + 3\tau_{m \max}^2} \cong \tau_{m \max} \sqrt{k^2 + 3} \quad (40)$$

The actual maximum may occur slightly before the fiber end (see Figs. 11 and 12), but for simplicity we assumed it is at the fiber end. The contribution of the tensile component σ_m is relatively small because typically $k < 1$.

We see that the critical debonding point in the bead-fiber interface is at the center of the bead closest to the fiber end, whereas in the matrix-bead interface it is at the bead far edge (at the fiber end). Such behavior was indeed observed in pullout and fragmentation tests of beaded fibers (Greenfeld et al., 2018). Given the bead-fiber and matrix-bead bonding strengths, σ_{bu} and σ_{mu} , respectively, the following criterion may be defined

$$C_i = \frac{\sigma_{mu}/\sigma_{m \text{vm}}}{\sigma_{bu}/\sigma_{b \text{vm}}} \cong \frac{\sigma_{mu} \sqrt{\sigma_b^2 + 3\tau_{b \max}^2}}{\sigma_{bu} \sqrt{\sigma_m^2 + 3\tau_{m \max}^2}} \cong \frac{\sigma_{mu} \tau_{b \max}}{\sigma_{bu} \tau_{m \max}} \quad (41)$$

When $C_i > 1$ the failure will start at the bead-fiber interface, whereas when $C_i < 1$ it will start at the matrix-bead interface. Intentional tuning of σ_{bu} and σ_{mu} can be applied to achieve a desirable failure mode (see example in Fig. 13).

A similar criterion can be defined to determine whether the fiber will break prior to the weakest interface. For example, if the bead-fiber interface is the weakest interface, the criterion is

$$C_f = \frac{\sigma_{fu}/\sigma_{f \max}}{\sigma_{bu}/\sigma_{b \text{vm}}} \cong \frac{\sigma_{fu} \sqrt{\sigma_b^2 + 3\tau_{b \max}^2}}{\sigma_{bu} \sigma_{f \max}} \cong \frac{\sigma_{fu} \sqrt{3} \tau_{b \max}}{\sigma_{bu} \sigma_{f \max}} \quad (42)$$

When $C_f > 1$ the failure will start at the interface, whereas when $C_f < 1$ the fiber will break first. As with beadless fibers, the elastic stress analysis typically results in $C_f > 1$, so that when interfacial loosening starts, the fiber stress is still significantly below its strength. However, plastic deformation of the matrix during failure can increase the fiber stress to a breaking point if its number of beads is larger than the critical number of beads (equivalent to the concept of critical length in beadless fibers) (Greenfeld et al., 2018).

The ultimate stresses identified in this section are calculated under the shear-lag modeling assumption that the composite stress and strain are averaged over a cross section through a large number of fibers. However, local stress concentrations in the bead, matrix and fiber induced by nearby fibers may change these ultimate stresses. Analysis of such inter-fiber load transfers, based on models developed by (Eitan and Wagner, 1991; Wagner and Eitan, 1993) and further elaborated by (Grubb et al., 1995), is provided in the Supporting Information. The main conclusion from this analysis is that, when considering multiple nearby fibers, each with a different staggering offset (fixed or random) with respect to the affected fiber, such stress concentrations are smoothed, consistent with the shear-lag averaging approximation.

As suggested, the failure mode can be tuned by selection of material and interfacial properties. One way to accomplish this is to modify the matrix-bead interfacial strength by applying coating on the beaded fibers prior to their embedding in the matrix. For example, if a release agent is applied (increasing σ_{bu}/σ_{mu} in Fig. 13), the matrix-bead interface will be weakened and will likely debond first. However, in contrast to the catastrophic failure that happens upon fiber interfacial

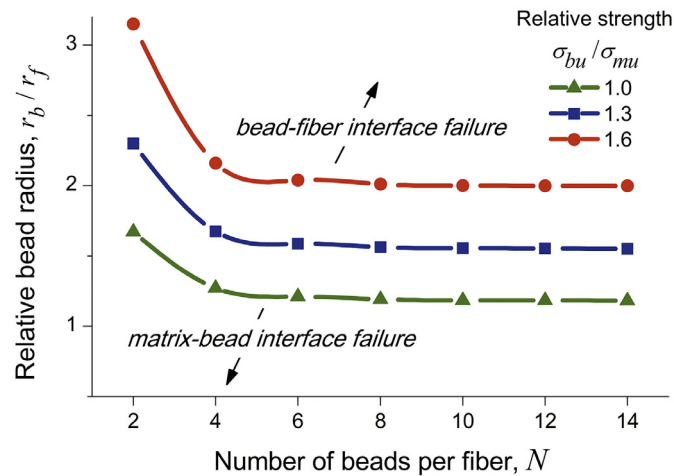


Fig. 13. Effect of interfacial tuning on failure mode. Regions of interfacial failure mode mapped on the parametric space of the bead radius and the number of beads. The curves are given by $C_i = 1$ (Eq. (41)) for 3 values of the bead-fiber and matrix-bead relative interfacial strength, $\sigma_{bu} / \sigma_{mu}$. Above each curve a bead-fiber interfacial failure is expected, whereas below it a matrix-bead interfacial failure is expected. The other parameters are as in Fig. 5. The maximal fiber volume fraction is taken for each case (Eq. 2).

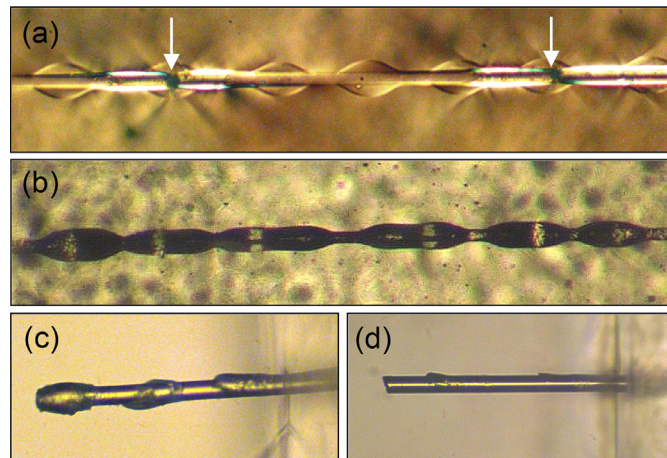


Fig. 14. Failure of a beaded fiber composite. Single beaded glass fiber embedded in epoxy matrix, subjected to gradually increasing longitudinal stress. (a) Birefringence image of the stress on beads; fiber breaks are indicated by arrows. (b) Plastic deformation of the matrix under beads pressure, subsequent to bead-matrix debonding. (c) Pullout of beaded fiber. (d) Pullout of fiber from its beads.

debonding, in the case of matrix-bead debonding the fiber remains anchored in the matrix (that is, topologically locked). Furthermore, the pressure induced by the matrix on the bead slope generates radial inward pressure in the bead, enhancing the bead grip on the fiber. If the fiber strength is exceeded, the fiber will break and the beads will push against the matrix causing plastic deformation. Eventually, a crack will propagate through the matrix, and fiber sections with or without beads will pull out from the matrix. This train of events, observed experimentally (Fig. 14) for same bead and matrix material, has the potential to improve toughness without harming strength (Greenfeld et al., 2018).

8. Conclusions

The complex structure of a beaded fiber composite and the motivation for its use are described in this study, with focus on the elastic stress profiles that develop under load and the composite stiffness. The proposed model extends the classic Cox shear lag theory of fiber composites to beaded fiber composites, and is substantiated by finite element analysis. The addition of beads on fibers, and the new bead-matrix interface, significantly increase the model level of complexity. The resulting stresses incur periodic perturbations induced by the beads, expressed by the classic Hill's differential equation.

As in the shear lag model for beadless fibers, the current model is approximate, as it assumes perfect 2D axisymmetry, neglects the radial and circumferential stresses, and does not predict stress concentrations at the fiber ends. Yet, these approximations should not impact the prediction of the composite stiffness, and the model remains an excellent tool for

understanding the elastic behavior of this structure. Future work may extend this study to larger scale finite element models and to plastic and fracture behavior under ultimate loads.

The model shows that, if the beads are stiffer than the matrix, the stress transfer from the matrix to the fiber is more efficient than in beadless fibers due to an anchoring effect. This is evidenced through the elevated interfacial stress at bead locations and the higher fiber stress. Consequently, the composite stiffness is raised, particularly for higher bead stiffness and larger beads. Conversely, if the beads are less stiff than the matrix, the composite can be made more compliant and possibly more ductile.

The composite strength is dominated by the weakest link in the structure, whether fiber, bead, matrix or any of their interfaces, and the fracture mechanisms may include interfacial debondings, fiber pullouts, bead pullouts and fiber breaks. The strength of the bonding layer between the bead and matrix can be tuned by coating, allowing it to debond first but without losing anchoring. The ensuing compressive plastic deformation of the matrix by the beads likely improves the composite toughness without harming its strength. Further experimental and theoretical research is anticipated in characterizing the failure modes of beaded fiber composites, and their impact on the composite strength and toughness.

Acknowledgments

The authors would like to acknowledge support from the G.M.J. Schmidt Minerva Centre of Supramolecular Architectures at the Weizmann Institute, and the generosity of the Harold Perlman family. C.R. was supported by the European Union's Horizon 2020 research and innovation ITN programme under the Marie Skłodowska-Curie grant agreement No 722626 Fi-BreMoD. H.D.W. is the recipient of the Livio Norzi Professorial Chair in Materials Science. We thank Prof. Bingbing An for his support in finite element analysis.

Supplementary material

Supplementary material associated with this article can be found, in the online version, at doi:[10.1016/j.jmps.2018.12.020](https://doi.org/10.1016/j.jmps.2018.12.020).

References

- Atkins, A.G., 1975. Intermittent bonding for high toughness—High-strength composites. *J. Mater. Sci.* 10, 819–832.
- Bagwell, R.M., Wetherhold, R.C., 2003. Improvement in fracture toughness of an epoxy/copper composite through the use of various end shaped fibers. *Mater. Sci. Eng. A* 361, 294–301.
- Barthelat, F., Yin, Z., Buehler, M.J., 2016. Structure and mechanics of interfaces in biological materials. *Nat. Rev. Mater.* 1, 1–16.
- Beyerlein, I.J., Zhu, Y.T., Mahesh, S., 2001. On the influence of fiber shape in bone-shaped short-fiber composites. *Compos. Sci. Technol.* 61, 1341–1357.
- Cottrell, A.H., 1964. Strong solids. *Proc. R. Soc. Lond. A* 282.
- Cox, H.L., 1952. The elasticity and strength of paper and other fibrous materials. *Brit. J. Appl. Phys.* 3, 72.
- de Gennes, P.G., Brochard-Wyart, F., Quere, D., 2004. Capillarity and Wetting Phenomena—Drops, Bubbles, Pearls, Waves. Springer-Verlag New York, Inc.
- Eitan, A., Wagner, H.D., 1991. Fiber interactions in 2-dimensional composites. *Appl. Phys. Lett.* 58, 1033–1035.
- Gao, X., Jensen, R.E., McKnight, S.H., Gillespie, J.W., 2011. Effect of colloidal silica on the strength and energy absorption of glass fiber/epoxy interphases. *Compos. Part A Appl.* 42, 1738–1747.
- Greenfeld, I., Sui, X.M., Wagner, H.D., 2016. Stiffness, strength, and toughness of electrospun nanofibers: Effect of flow-induced molecular orientation. *Macromolecules* 49, 6518–6530.
- Greenfeld, I., Wagner, H.D., 2015. Nanocomposite toughness, strength and stiffness—The role of filler geometry. *Nanocomposites* 1, 3–17.
- Greenfeld, I., Zhang, W., Sui, X., Wagner, H.D., 2018. Intermittent beading in fiber composites. *Compos. Sci. Technol.* 160, 21–31.
- Grubb, D.T., Li, Z.F., Phoenix, S.L., 1995. Measurement of stress-concentration in a fiber adjacent to a fiber break in a model composite. *Compos. Sci. Technol.* 54, 237–249.
- Hill, G.W., 1877. On the part of the motion of the lunar perigee which is a function of the mean motions of the sun and moon. reprinted. *Acta Mathematica* 28 (1886), 1881–1836.
- Jensen, R.E., McKnight, S.H., 2006. Inorganic-organic fiber sizings for enhanced energy absorption in glass fiber-reinforced composites intended for structural applications. *Compos. Sci. Technol.* 66, 509–521.
- Kelly, A., 1970. Interface Effects and Work of Fracture of a Fibrous Composite. *Proc. Royal Soc. London Series A* 319, 95.
- Lei, H.F., Zhang, Z.Q., Liu, B., 2012. Effect of fiber arrangement on mechanical properties of short fiber reinforced composites. *Compos. Sci. Technol.* 72, 506–514.
- Magnus, W., Winkler, S., 1979. Hill's Equation. Dover, New York.
- Phanthien, N., 1981. Effective elastic-moduli of enlarged-end-fiber-reinforced solids. *Fibre Sci. Technol.* 14, 241–250.
- Piggott, M., 2002. Load Bearing Fibre Composites, 2nd ed. Kluwer Academic Publishers.
- Ritchie, R.O., 2011. The conflicts between strength and toughness. *Nat Mater.* 10, 817–822.
- Sui, X.M., Greenfeld, I., Cohen, H., Zhang, X.H., Li, Q.W., Wagner, H.D., 2016. Multilevel composite using carbon nanotube fibers (CNTF). *Compos. Sci. Technol.* 137, 35–43.
- Sui, X.M., Wagner, H.D., 2009. Tough nanocomposites: the role of carbon nanotube type. *Nano Lett.* 9, 1423–1426.
- Sun, X.Y., Zhang, Z.Q., Xu, Y.J., Zhang, Y.W., 2015. An elastic model for bioinspired design of carbon nanotube bundles. *Acta Mech Sinica-Prac* 31, 205–215.
- Timoshenko, S.P., Goodier, J.N., 1970. Theory of Elasticity, 3rd ed. Mcgraw-Hill.
- Tsai, H.C., Arocho, A.M., Gause, L.W., 1990. Prediction of fiber matrix interphase properties and their influence on interface stress, displacement and fracture-toughness of composite-material. *Mater. Sci. Eng. A* 126, 295–304.
- Wagner, H.D., Eitan, A., 1993. Stress-concentration factors in 2-dimensional composites—Effects of material and geometrical parameters. *Compos. Sci. Technol.* 46, 353–362.
- Wegst, U.G.K., Bai, H., Saiz, E., Tomsia, A.P., Ritchie, R.O., 2015. Bioinspired structural materials. *Nat. Mater.* 14, 23–36.
- Weiner, S., Wagner, H.D., 1998. The material bone: Structure-mechanical function relations. *Annu. Rev. Mater. Sci.* 28, 271–298.
- Wetherhold, R.C., Corjon, M., Das, P.K., 2007. Multiscale considerations for interface engineering to improve fracture toughness of ductile fiber/thermoset matrix composites. *Compos. Sci. Technol.* 67, 2428–2437.

- Wetherhold, R.C., Lee, F.K., 2001. Shaped ductile fibers to improve the toughness of epoxy-matrix composites. *Compos. Sci. Technol.* 61, 517–530.
- Yang, L., Greenfeld, I., Wagner, H.D., 2016. Toughness of carbon nanotubes conforms to classic fracture mechanics. *Sci. Adv.* 2, 1–8.
- Zhang, Z.Q., Liu, B., Huang, Y., Hwang, K.C., Gao, H., 2010. Mechanical properties of unidirectional nanocomposites with non-uniformly or randomly staggered platelet distribution. *J. Mech. Phys. Solids* 58, 1646–1660.
- Zhu, Y.T., Valdez, J.A., Shi, N., Lovato, M.L., Stout, M.G., Zhou, S.J., Butt, D.P., Blumenthal, W.R., Lowe, T.C., 1998. A composite reinforced with bone-shaped short fibers. *Scripta Mater.* 38, 1321–1325.